# Abu Roash F reservoir hydrocarbon potential, Western Desert, Egypt

Mohamed Said RADWAN[1,2,*] ⓘ, Mohamed GOBASHY[2] ⓘ,
Said DAHROUG[2] ⓘ, Samir RASLAN[1]

[1] Exploration department, Ministry of Petroleum and Mineral Resources,
  Nasr City, Cairo, Egypt

[2] Cairo University, Giza, Egypt

**Abstract:** The Western Desert of Egypt is recognized for its significant potential in oil and gas reserves, making it a prominent hydrocarbon-producing area with conventional reservoirs. Recent findings from various wells suggest that unconventional reservoirs in the Western Desert may hold considerable promise. The primary objective of this study was to explore this potential. Accordingly, a comprehensive and multidisciplinary approach has been employed to assess the Abu Roash/F (AR/F) reservoir. The methodology involved meticulously examining formation characteristics and integrating borehole images with existing core data and thin sections. This integration aimed to analyse and interpret the lithofacies of the reservoir, with a specific focus on identifying fractures and decoding potential diagenesis effects. As a result, we successfully identified wells exhibiting optimal reservoir quality, unveiling the presence of fractured dolomite or vuggy dolomite in wells containing promising oil and gas pay intervals. Notably, some wells displayed low porosity (3%), yet seismic attribute maps in their vicinity indicated a high density of fractures. This underscores the importance of combining borehole images with seismic attributes to evaluate carbonate formations effectively. The fractures, predominantly oriented NW–SE, were found to be associated with deformation zones. Our findings emphasize the critical role of this integrated approach in unlocking the full potential of hydrocarbon reservoirs in the Western Desert.

**Key words:** Western Desert, Upper Cretaceous, Abu Roash F, unconventional reservoirs

## 1. Introduction

The Western Desert is one of Egypt's principal hydrocarbon provinces (*Hantar, 1990; Meshref, 1990*). Most of the production came from conventional reservoirs, with only a few wells producing from unconventional ones. However, several wells suggest that the unconventional reservoirs in the Western Desert may hold great promise (*Abd El-Aal and Moustafa, 1988*). The unconventional reservoirs always act as both source and reser-

---

145

voir rocks, and they always attain very low permeability, requiring hydraulic fracturing for increased production. The study area (Fig. 1) is located in the central and eastern parts of the Western Desert. Our investigation concentrated on AR/F member, which is regarded as one of the primary source rocks (*Meshref, 1990; Abdelmaksoud et al., 2019*) in the Western Desert. Many wells have penetrated the AR/F member in the Western Desert and encountered oil and gas shows, but these wells have not yet been tested for production. This observation prompted us to comprehensively analyse and interpret some of the Western Desert's potential areas.
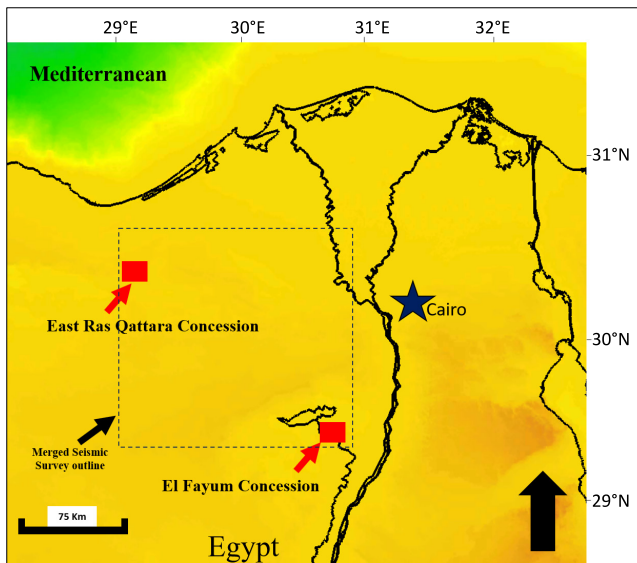


Fig. 1. Location map of the study areas, East Ras Qattara and El Fayum concessions, dashed box represents the outline of the EUG Western Desert merged volume (*Osman et al., 2022*).

The primary objective of this study was to integrate multidisciplinary approaches to evaluate the AR/F reservoir, including Borehole imaging analysis, and petrophysical, geological, and geophysical interpretation. The integrated approach (*Osman et al., 2022*) was executed by maximizing the contribution of all significant and available data and information to ensure that all aspects of interpretation are appropriately considered. It is important to perform a detailed structural model based on subsurface geological information (*Abdelmaksoud et al., 2019*) since the current energy industry

seeks to improve subsurface exploration through accurate assessment and competent production, and utilizing the electrical log is the best way to unlock hydrocarbon development from unconventional reservoirs.

To evaluate the source rock acting as a reservoir (unconventional reservoirs), it is necessary to evaluate the intragranular kerogen or organic porosity because it is considered an additional component of the source rock reservoir as shown in Fig. 2. Unlike conventional porosity associated with conventional reservoirs, the organic porosity system in source rock reservoirs is distinctive because it is created by thermal maturation and conversion of organic matter into hydrocarbons (*Galford et al., 2013*). The amount formed in the bulk rock is proportional (*El-Sabbagh et al., 2011*) to the current volume of solid kerogen. Thus, organic porosity contributes to total reservoir hydrocarbon storage capacity and may be the primary storage mechanism in some productive source rock reservoirs (*Ibrahim and Abdel Aziz, 1995; Lüning et al., 2004; Zobaa et al., 2011*).
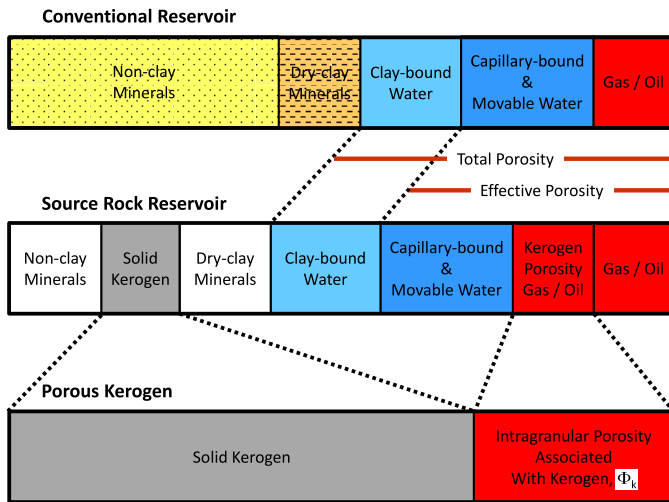


Fig. 2. Intragranular kerogen porosity introduces a new component of effective porosity not present in conventional reservoirs (*Galford et al., 2013*).

## 2. Geological setting

The Western Desert in Northern Egypt contains multiple active petroleum systems, as indicated by *Meshref (1990)*, with abundant source rocks rich

in organic matter located within the extended rift basins, as noted by *Katz (1995)*.

The Upper Cretaceous rock units within the Northern Western Desert can be categorized into three primary sequences: Bahariya, Abu Roash (AR), and Khoman formations. The Abu Gharadig sedimentary basin's Cretaceous sequence averages approximately 2000 metres in thickness (*Meshref, 1990*). Within the Abu Roash (AR) formation, which includes shallow to deeper marine carbonates, there are observable alternating transgression and regressive stages. Dolomitized limestone exhibits fracture porosity, while shale and sandstone intercalations contribute to the composition of shallow deposits. The AR formation (*Abdelmaksoud et al., 2019*) is further characterized by seven lithostratigraphic members (AR/G, AR/F, AR/E, AR/D, AR/C, AR/B, and AR/A) spanning the Santonian through the Late Cenomanian periods. During this period, the AR/G, AR/E, AR/C, and AR/A members contain varying quantities of detritus, while the AR/B, AR/D, and AR/F members are identified as clean carbonates (*Bayoumi and Lofty, 1989; Hantar, 1990; EGPC, 1992*). Figure 3 illustrates the stratigraphical column in the Northern Egyptian Western Desert.

AR/F source/reservoir rock was deposited during the Cretaceous. Regional subsidence associated with Neo-Tethyan rifting occurred across the North African margin during the Cretaceous/Cenomanian, the entire northern African plate was subject to a marine transgression, which culminated in the Turonian when a seaway connected Neo-Tethys to the South Atlantic (*Philip et al., 1993*). AR/F limestones are thought to be the primary source of rock in the western desert, according to researchers (*Abdelmaksoud et al., 2019*). Figure 4 shows the regional isopach thickness map of AR formation across the Western Desert showing basinal areas.

The Northern Western Desert displays a prevalence of faults oriented along the ENE–WSW direction and a distinct pattern of faults aligned NW–SE, signifying the impact of regional strike-slip activities and multiple phases of rifting (*Abd El-Aal and Moustafa, 1988*). Within the Northern Western Desert, there is a significant sedimentary sequence dating from the Late Jurassic to the Early Cretaceous, shaped by two notable sinistral and dextral shear tectonic events linked to the opening of the Atlantic Ocean. These events involve the left lateral movement of Africa against Eurasia in the Late Jurassic to Early Cretaceous, leading to the eastward displace-
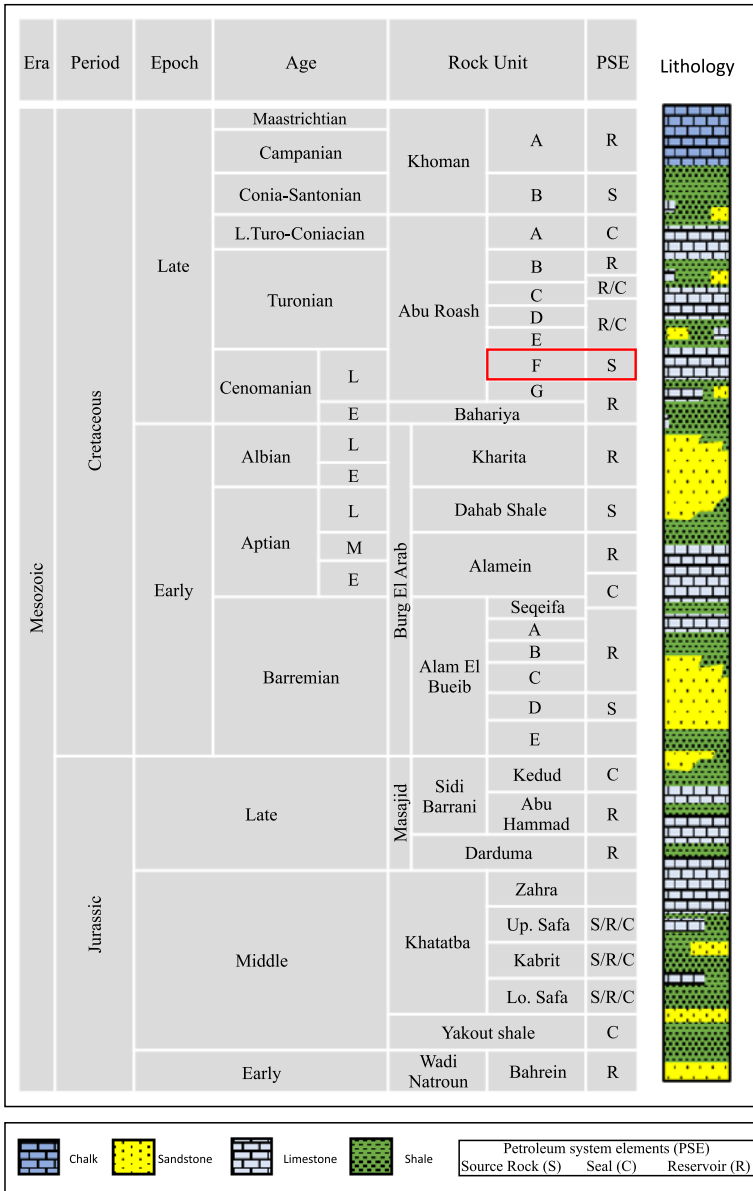
| Era | Period | Epoch | Age | | Rock Unit | | | PSE | Lithology |
|---|---|---|---|---|---|---|---|---|---|
| Mesozoic | Cretaceous | Late | Maastrichtian | | Khoman | A | | R | |
| | | | Campanian | | | | | | |
| | | | Conia-Santonian | | | B | | S | |
| | | | L.Turo-Coniacian | | Abu Roash | A | | C | |
| | | | Turonian | | | B | | R | |
| | | | | | | C | | R/C | |
| | | | | | | D | | R/C | |
| | | | | | | E | | | |
| | | | Cenomanian | L | | F | | S | |
| | | | | | | G | | | |
| | | | | E | Bahariya | | | R | |
| | Cretaceous | Early | Albian | L | Burg El Arab | Kharita | | R | |
| | | | | E | | | | | |
| | | | Aptian | L | | Dahab Shale | | S | |
| | | | | M | | Alamein | | R | |
| | | | | E | | | | C | |
| | | | Barremian | | | Seqeifa | | | |
| | | | | | | Alam El Bueib | A | R | |
| | | | | | | | B | | |
| | | | | | | | C | | |
| | | | | | | | D | S | |
| | | | | | | | E | | |
| | Jurassic | Late | | | Masajid | Sidi Barrani | Kedud | C | |
| | | | | | | | Abu Hammad | R | |
| | | | | | | Darduma | | R | |
| | | Middle | | | | Khatatba | Zahra | | |
| | | | | | | | Up. Safa | S/R/C | |
| | | | | | | | Kabrit | S/R/C | |
| | | | | | | | Lo. Safa | S/R/C | |
| | | | | | | Yakout shale | | C | |
| | | Early | | | | Wadi Natroun | Bahrein | R | |

Legend: Chalk, Sandstone, Limestone, Shale

Petroleum system elements (PSE): Source Rock (S)  Seal (C)  Reservoir (R)

Fig. 3. Stratigraphic column of the Western Desert after (*Schlumberger, 1972 and 1995*) which highlights the AR/F member.

ment of Africa relative to Eurasia. Additionally, there was a right lateral movement during the Late Cretaceous to Palaeocene, coinciding with the opening of the North Atlantic Ocean, causing Africa to move westward against Eurasia (*Abd El-Aal and Moustafa, 1988*).
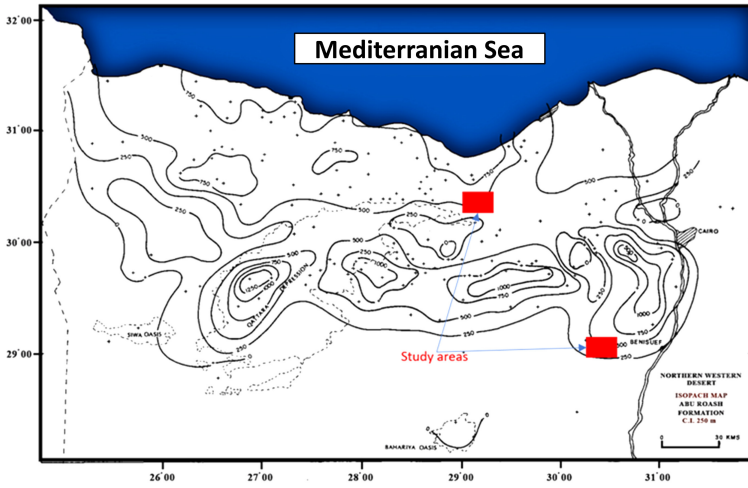


Fig. 4. Regional isopach thickness map of AR formation across the Western Desert showing Basinal areas (modified after *Hantar, 1990*).

The geological history and successive structural events during the Tertiary, Cretaceous, and Jurassic periods contributed to the development of EW and ENE-WSW trending faults and fractures in the Northern Western Desert (*Dolson et al. 2001*).

## 3. Methodology

The methodology employed in this investigation (depicted in Fig. 5) incorporated the synthesis of formation evaluation and borehole images for three wells, coupled with existing core data and thin sections. This comprehensive approach aimed to analyse and interpret reservoir lithofacies, decipher potential diagenesis effects, and particularly emphasize fracture identification. Additionally, structural mapping was carried out on the available 3D seismic data by combining seismic attributes such as edge detection, coherence, and minimum curvature to identify fractures.
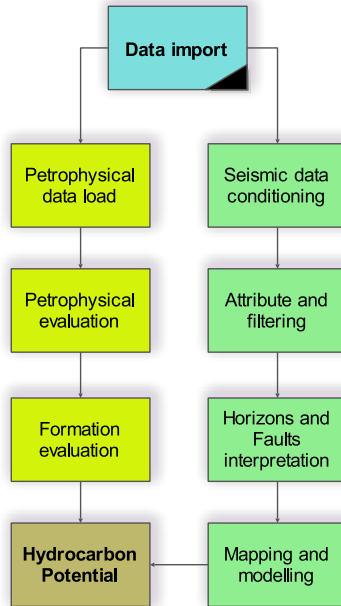
Fig. 5. The general framework of the undertaken workflow in this study.

## 3.1. Seismic data analysis

The Egypt Upstream Gateway (EUG) conducted a comprehensive post-stack volume, as illustrated in Fig. 1, encompassing the Eastern region of the Egyptian Western Desert. This analysis served as a broader examination of play potential and the interconnections among existing fields. Through the integration of contemporary technologies such as image enhancement, bandwidth extension, and data matching, the merged post-stack volume revitalized numerous legacy datasets. By optimizing the bandwidth and resolution of the enhanced seismic data, merging datasets, and ensuring accurate matching of phase, amplitude, bandwidth, and reference datum during the imaging process, a coherent and interpretable seismic data volume was generated.

The inherent structural features evident in time-structured maps reveal the geological impact of local structural activities, mirroring the broader regional structuring that influences nearby areas (*Abu El-Ata, 1988*). Utilizing 3D seismic attributes proves highly effective in identifying faults and

fracture zones that extend beyond the resolution of seismic measurements. Seismic attributes are divided into two categories, namely physical and geometrical characteristics (*Sheriff and Geldart, 1995*). In our context, evidence from the geometrical seismic attribute, specifically variance, is employed to guide the identification of both minor and major faults and fracture patterns. This information can then be cross-referenced with the outcomes of traditional interpretation, serving as a quality control measure to identify and rectify any potential human errors arising from the conventional interpretation of seismic reflectivity.

## 3.2. Well-logging data analysis

Four well-logging data were available for our integrated analysis and qualitative interpretation, these wells logging include open-hole triple combo (Gamma-ray, resistivity, density, neutron), sonic logs, mud logs, Borehole micro-resistivity imaging, and nuclear magnetic resonance (NMR). Using these downhole measurements, estimations of petrophysical properties like porosity, water saturation, and Net pay have been made.

Triple combo logs with NMR and sonic data were used in the detailed petrophysical analysis of the potential wells. The deterministic petrophysical analysis began with data quality control and progressed to the volume of shale calculations, porosity computations (both total and secondary), water saturation determination, lithology computation, and net reservoir and net pay calculation. The standard evaluation is based on various literature (*Archie 1942; Schlumberger, 1972 and 1995; Dresser Atlas, 1982; Asquith and Gibson, 1982; Crain, 1986; Rider, 1996; Krygowski, 2003*).

Because of the effect of solid kerogen on the density log, which leads to an overestimation of porosity, NMR data were used to correct the porosity computed from the density log. While the hydrogen in kerogen has a very fast relaxation time, it is undetectable by NMR logs. In our study, we calculated kerogen volume using the difference between available NMR porosity and density porosity (*Steiner et al., 2016*):

$$V_k = \frac{\rho_m - \rho_l}{\rho_m - \rho_k} - \frac{\phi_{\text{NMR}}\left(\rho_m - \rho_l\right)}{\text{HI}\left(\rho_m - \rho_k\right)}, \tag{1}$$

$V_k$ is kerogen volume, $\rho_m$, $\rho_l$, and $\rho_k$ are matrix, fluid, and kerogen densities, and HI is the hydrogen index for fluid, $\phi_{\text{NMR}}$ is NMR porosity.

In the absence of NMR data total organic carbon (TOC) needs to be determined, two methodologies were used in our study:

a) $\Delta \log$ R methodology of *Passey et al. (1990)* based on using porosity and resistivity measurements. This method assumes that in a water-filled non-source rock interval, changes in porosity as measured by sonic should be reflected by an equivalent change in resistivity and that any deviation from this rule is due to the presence of organics which was used to determine (TOC) based on the apparent separation between the resistivity and porosity logs when properly scaled, the scaling of curves will be 50 $\mu$sec/ft or 164 $\Delta$sec/feet per one resistivity cycle.

$$\Delta \log \text{R} = \frac{\log_{10}\left(\frac{\text{RLLD}}{\text{R}_{\text{base}}}\right) + (\Delta t - \Delta t_{\text{base}})}{164} \,, \tag{2}$$

$$\text{TOC} = 10^{(2.297 - 0.168\,\text{Lm})} \cdot \Delta \log \text{R} \,, \tag{3}$$

RLLD is deep resistivity, $\Delta t$ is the slowness value from sonic, $\text{R}_{\text{base}}$ is resistivity, and $\Delta t_{\text{base}}$ is the slowness value in non-source rocks. Lm is the amount of level organic metamorphism.

b) Schmoker method (*Schmoker and Hester, 1983*) – KHC – Schmoker method relies on the density measurement (due to the low density of organics) to compute TOC:

$$\text{TOC} = \frac{\text{A}}{\text{RHOB}} - \text{B} \,, \tag{4}$$

RHOB is bulk density, and A and B are constants that can be derived by using a solver.

After the estimation of TOC, the volume of kerogen can be computed by the following equation:

$$V_k = \rho_b \frac{\text{TOC}}{\rho_k} \,, \tag{5}$$

$V_k$ is kerogen volume, $\rho_b$ and $\rho_k$ are bulk and kerogen densities. The corrected porosity can be computed by the following equation:

$$\phi_c = \phi_a - V_k \phi_k \,, \tag{6}$$

$\phi_c$ is corrected porosity, $\phi_a$ is apparent calculated porosity and $\phi_k$ is kerogen porosity which is a function of the maturity of AR/F member.

Borehole micro-resistivity images are regarded as one of the most effective tools for determining fracture orientation and type. Fracture types are classified according to the material used to fill the fractures and can be divided into two categories: 1-conductive fractures and 2-resistive fractures, the former are fractures filled with clay or water-based mud that invaded open fractures and replaced oil or gas, whereas the latter are fractures filled with cemented materials (e.g., anhydride, silica, and calcite). Previous work published by (*Luthi and Souhaite, 1990*) illustrated the relationship between the fracture aperture and measured excess current as the tool crosses the fractures by the following equation:

$$W = c \cdot A \cdot Rm \cdot b \cdot R_{xo}^{1-b}, \tag{7}$$

where, $W$ = fracture aperture in (mm), $A$ = excess current ($\mu$A mm/v), $Rm$ = resistivity of mud (ohm.m), $R_{xo}$ = flushed resistivity, while $b$ and $c$ are parameters related to different tools (e.g., related to different acquisition companies).

## 4. Results

The well-X was investigated using an image log where the image-based interpretation reveals the existence of several open fractures (Fig. 6), which in borehole images appear as conductive (dark-coloured) fractures because drilling mud typically penetrates the fracture opening and forms a thin, conductive sheet with a resistivity that is always lower than the resistivity of the rock matrix surrounding it. There are two types of fractures discovered in the well: bedbound fractures, which are short fractures that truncate at bed boundaries, and continuous conductive fractures. Continuous fractures typically have a higher degree of connectivity than bed-bound fractures, which increases their permeability. Bed-bound fractures are always short in length, small in height, and have a tiny aperture, whereas continuous conductive fractures are always longer, higher in height, and larger in aperture. When fractures are not filled with clays, calcite, or zeolites, the fracture network forms the main conduits for fluid transmission and provides significant storage volume for the fluid, so it can be inferred that this fracture zone can act as a potential zone for hydrocarbon. Due to the scarcity of borehole images in many wells in the Western Desert, we relied on conventional
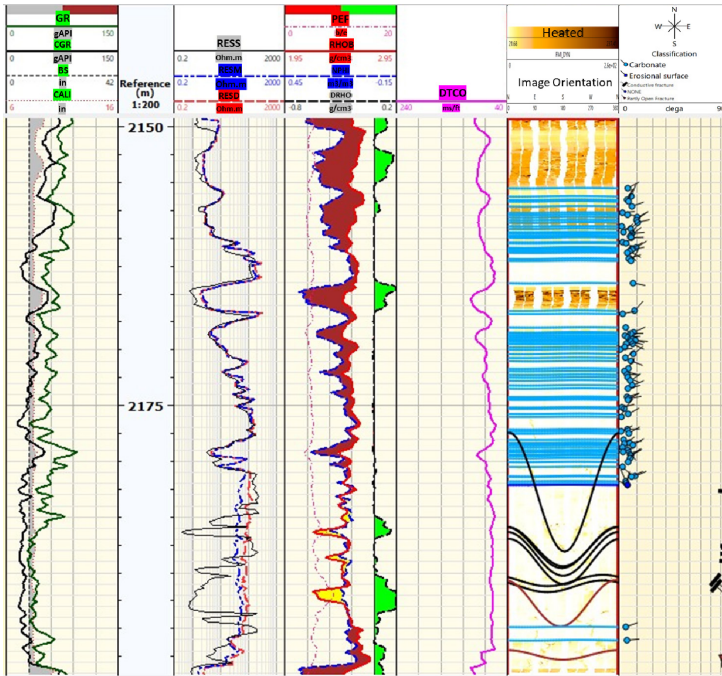
Fig. 6. Well logging layout with the processed static image displaying the presence of conductive fractures in Well -X, A: Track-1: Depth in meter, track-2: Caliper and bit size, track-3: Gamma-ray and computed gamma ray (CGR) which is gamma-ray without uranium, track-4: Resistivity curves, track-5: Density, neutron, track-6: Photoelectric factor, track-7: Processed static image.

well logging interpretation for fracture identification after calibration with borehole images. It was found in Well-X (Figs. 6 and 7) that the fracture zone is associated with:

1. High photoelectric factor (PEF) related to the presence of barite in mud.

2. Low flushed resistivity is due to the invasion of conductive mud.

3. High caliper reading due to invasion.

4. When compared to rock without fractures, the high intensity of open fractures can result in a lower bulk density measurement, which correlates with aperture size.

Several promising wells were petrophysical analysed for identifying potential zones in AR/F member. It was mandatory to correct the effect of
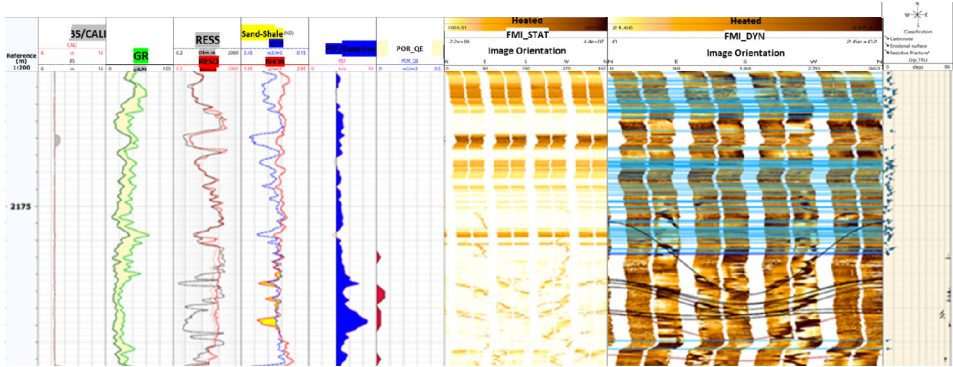
Fig. 7. Well-X: AR/F reservoir fracture characterization (orientation, distribution, and frequency), based mainly on micro-resistivity images. Track-1: Depth in meters, track-2: Caliper and bit size, track-3: Gamma-ray and computed gamma ray (CGR) which is gamma-ray without uranium, track-4: Resistivity curves, track-5: Density and neutron, track-6: Photoelectric factor, track-7: fracture density, track-8: processed static image, track-9: fracture aperture, track-10: dynamic image, track-11: True dip.

kerogen during porosity computation to obtain a precise porosity for water saturation computation. The porosity in wells with acquired NMR data was corrected using the previously discussed equation (1); it can be seen in Fig. 7 that the difference between porosity from the density log and porosity from NMR is related to kerogen volume in the rock, which was later used for correction of porosity computed from density. The predicted TOC from the Passey method was much better compared to Schomker, we found good agreement between the TOC predicted and actual TOC value in the blind well-H, which was not used in prediction, as shown in (Fig. 8).

Figure 9 illustrates the petrophysical examination of well-X, indicating potential hydrocarbons in the lower section of the AR/F Member. This zone exhibits noteworthy secondary porosity, reaching 10%, a water saturation range of $15-30\%$, and a substantial effective porosity of 20%, along with observable oil and gas indications. Identified as a fractured zone through borehole image analysis, this zone displays elevated resistivity values with distinct resistivity differentials. The heightened resistivity is likely attributed to the existence of kerogen and oil within fractures. This fractured zone holds promise as a productive reservoir without the need for hydraulic fracturing.
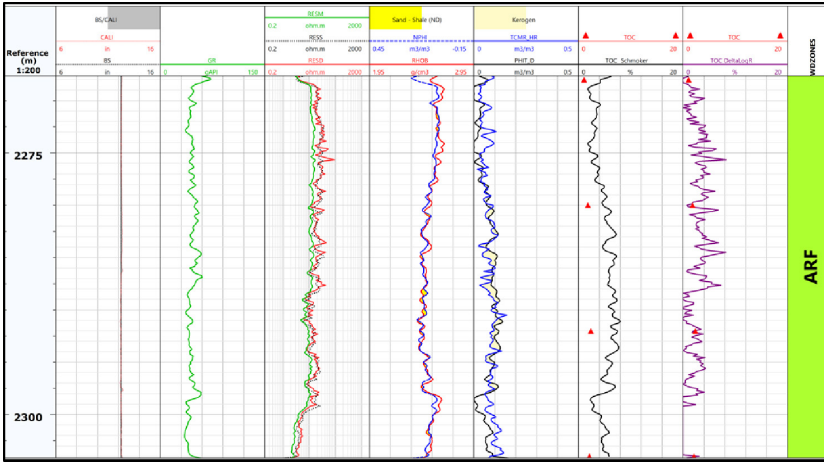
Fig. 8. Well-H: Well logging layout displaying the difference between NMR porosity and density porosity with predicted TOC with two methods used.
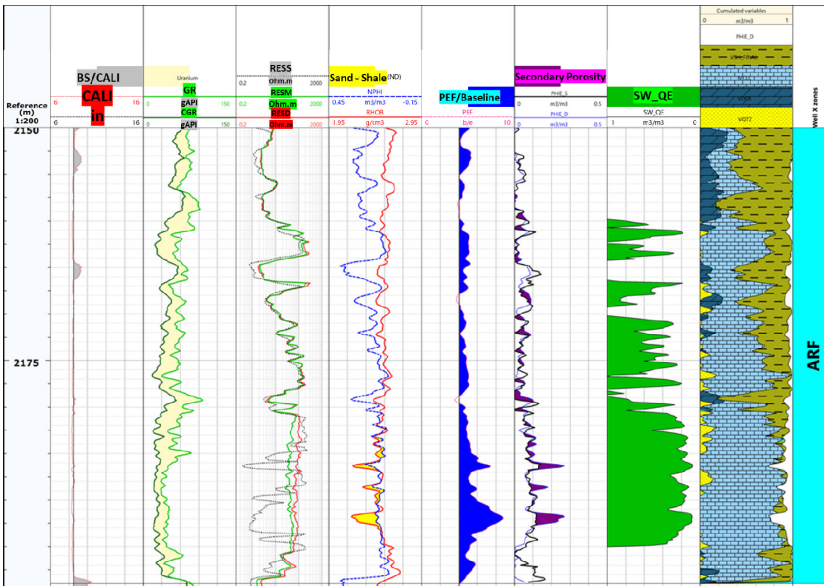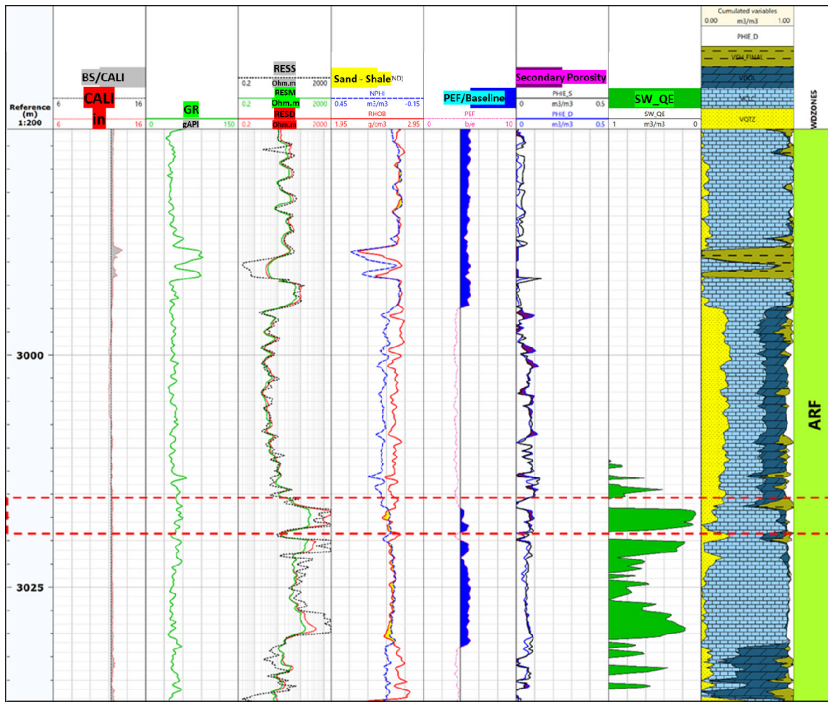


Fig. 9. Well-X: Petrophysical interpretation layout. Track-1: Depth in meter, track-2: Caliper and bit size, track-3: Gamma-ray and computed gamma ray, track-4: Resistivity curves, track-5: Density and neutron, track-6: Photoelectric factor, track-7: Porosity and secondary porosity, track-8: water saturation, track-9: Lithology obtained from lithology computation, track-10: Zonation.

Well-Y is in the same field as Well-X shows that it has a very low secondary porosity density compared to Well-X, implying that its quality is inferior to Well-X. Unfortunately, it doesn't have a borehole image for fracture characterization, but from the well logging pattern, it seems that it is tighter compared with Well-X. High resistivity is related to the presence of kerogen, which leads to low water saturation.

Well-Z petrophysical interpretation (Fig. 10) shows a porosity range of 4 to 10%, a water saturation range of 15 to 30%, minor secondary porosity detected, and oil and gas show in the lower zone. Furthermore, the presence of kerogen could explain the high resistivity. Because of the high relative permeability of oil to water, the interval between 3012.5 and 3015 metres



Fig. 10. Well-Z: Petrophysical interpretation layout. Track-1: Depth in meter, track-2: Caliper and bit size, track-3: Gamma-ray, track-4: Resistivity curves, track-5: Density and neutron, track-6: Photoelectric factor, track-7: Porosity and secondary porosity, track-8: water saturation, track-9: Lithology obtained from lithology computation, track-10: Zonation.
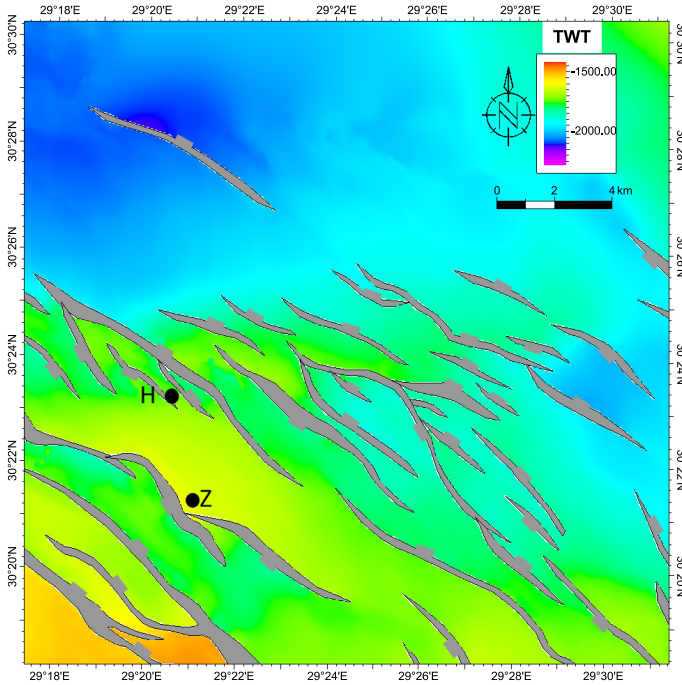
Fig. 11. TWT Structure contour map on the top of AR/F in the East Ras Qattara area to see the fault distribution and their relation with increasing fracture intensity in the study wells.

may have an annulus resistivity effect. The medium resistivity is the lowest because formation water moves faster from the flushed zone to the medium zone than oil.

The petrophysical evaluation for the evaluated wells proved that AR/F has an encouraging potential for hydrocarbon productivity. The results were integrated with the seismic interpretation (Figs. 11, 12, 13, 14, and 15) for the cretaceous levels and structure contour maps (obtained from seismic data analyses) to see the fault distribution and their relation with increasing fracture intensity in the studied wells. H and Z wells are very close to Cretaceous-oriented faults NW–SE (Figs. 11, 12, and 13), which justifies increasing the fracture intensity in well log analysis. Many seismic attributes analyses were performed on the top of the AR/F reservoir like variance maps (Fig. 13) for illustrating the fracture distribution in the study
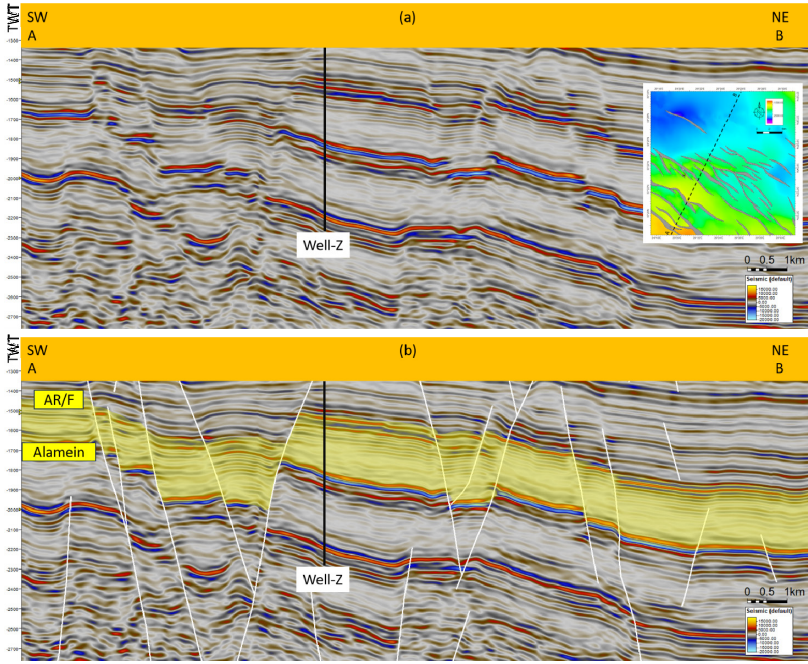
Fig. 12. Blank (a) and interpreted (b) SW–NE Seismic line passing through Well-Z in the East Ras Qattara area to see the fault distribution and their relation with increasing fracture intensity in the study wells.

area and linking the image results with seismic and well log data analyses. Figure 12 represents the seismic interpretation for the cretaceous levels to confirm the fracture zones around the study well and design production and development strategies.

## 5. Discussion

Our examination of the Upper Cretaceous AR/F reservoir within the Egyptian basins aligns with the conclusions drawn by *Farrag and Mahmoud (2022)* and *Osman et al. (2022)*. The AR/F member exhibits significant hydrocarbon potential, with fractures crucial in enhancing permeability and porosity in carbonate rocks. These fractures act as pathways for hydrocarbon migration and accumulation while also creating secondary porosity and storage capacity for hydrocarbons.
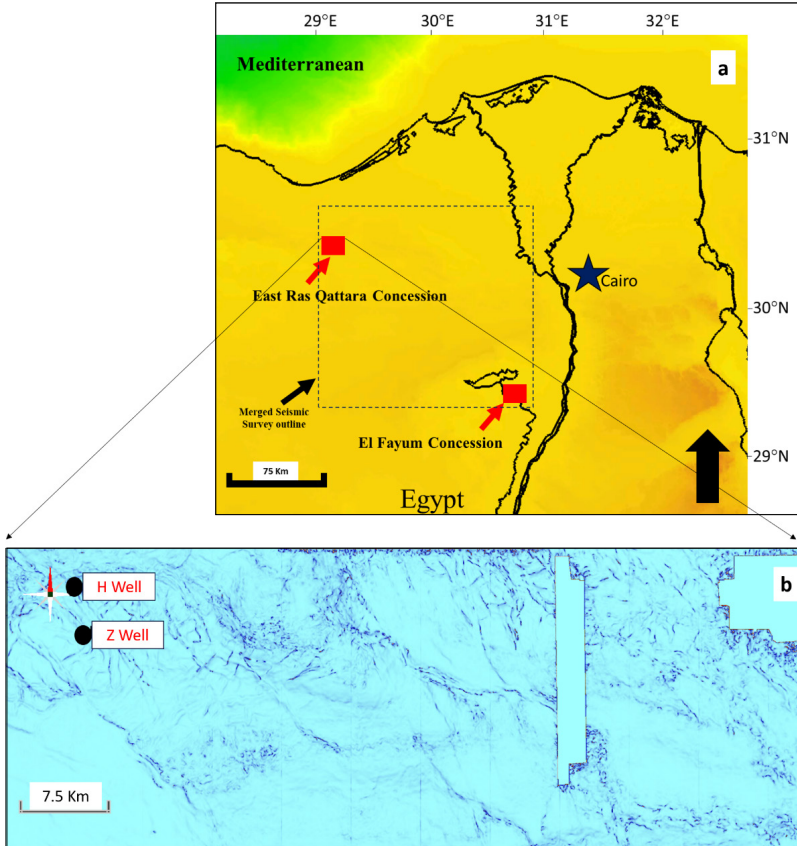
Fig. 13.  Location Map (a); Variance map (b) on the top of the AR/F reservoir which displays the orientation of the main faults and fracture networks in East Ras Qattara concession.

Fractured carbonate reservoir (ex. AR/F member) occurs in various geological settings, including faulted and folded regions, rift basins, and carbonate platforms.  Fractured carbonate reservoirs, such as those found in the Ghawar field in Saudi Arabia and the Permian Basin in the United States, are known for being among the largest and most productive oil and gas fields globally.

In the Egyptian Western Desert, AR/F reservoirs contribute significantly to hydrocarbon production in several fields, such as East Ras Qattara and El Fayum concessions.
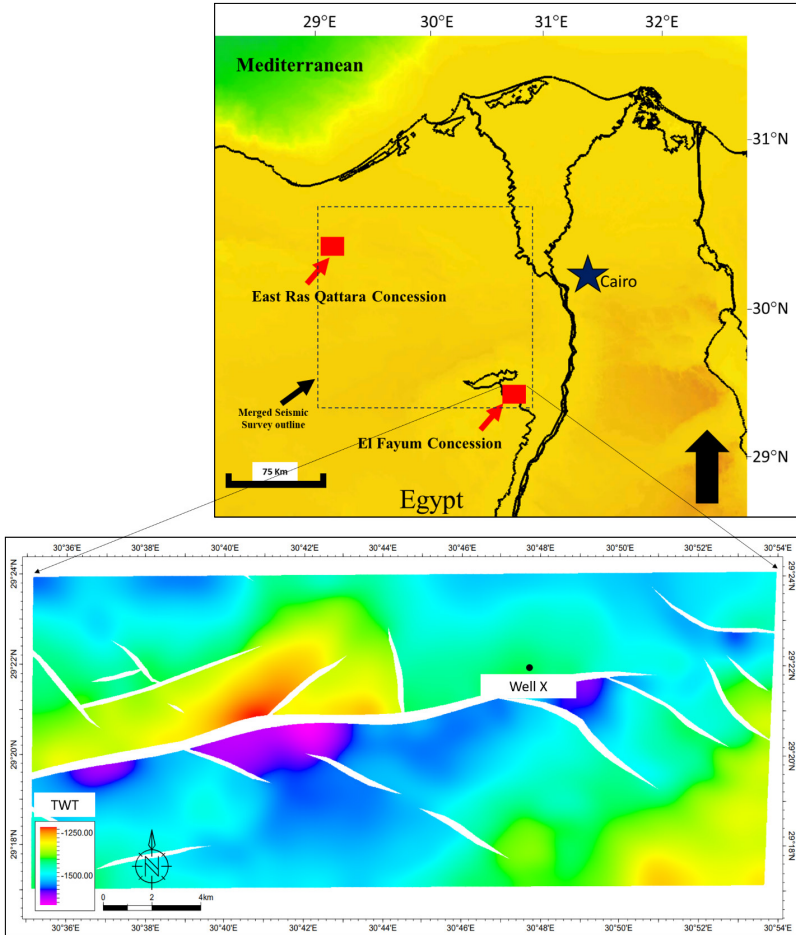
Fig. 14. Magnified TWT Structure contour map from the location map (El Fayum Concession) on the top of the AR/F reservoir in the area of Well-X to illustrate the fracture distribution around the Well-X area.

## 6. Conclusions

This work focuses on a comprehensive analysis that utilized a combination of seismic and geological data to delineate the hydrocarbon potential in the fractured Upper Cretaceous AR/F reservoir. This reservoir is characterized structurally by attached fractures to the NE–SW trending folds intersected
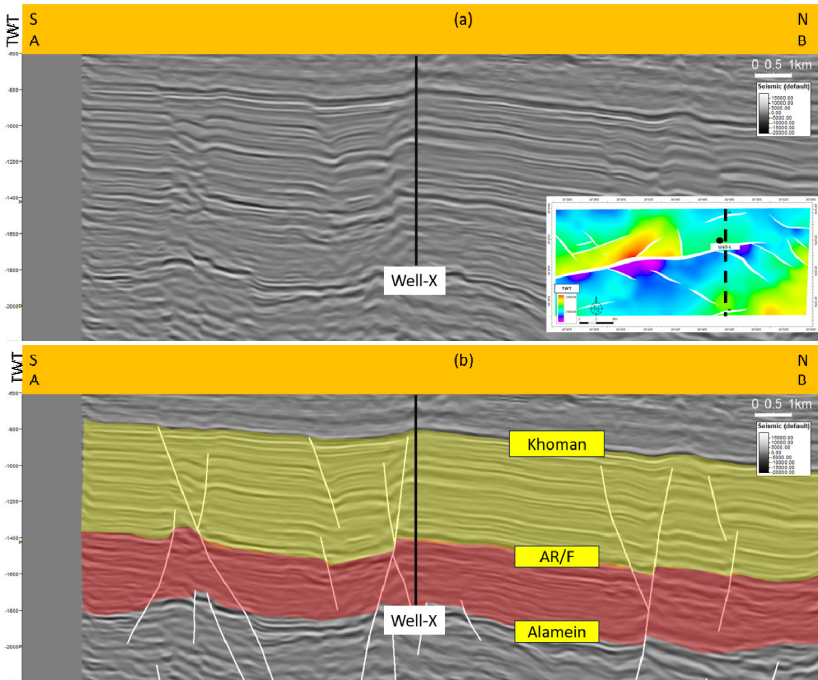
162

Fig. 15.  Blank (a) and interpreted (b) S–N Seismic line passing through Well-X in the Fayum area.

by NW–SE fault trends, offering 3-way closures bounded by nearby extensional faults that present promising exploration opportunities. The study's key findings are represented as the following:

- Borehole images unveil a discernible correlation between different features, fractures, and disruptions in seismic amplitude, as observed in the variant seismic cube. This correlation facilitates the identification of regions with a high density of fractures.

- The AR/F reservoir exhibits significant potential in various wells, and it is recommended to test these wells to unlock the unconventional reservoir's potential in Egypt.

- Borehole imaging is strongly recommended for future wells in the study area.

# References

Abd El-Aal A., Moustafa A. R., 1988: The structural framework of the Abu-Gharadig basin, Western Desert, Egypt. In: Proceedings of 9th EGPC Petroleum Exploration and Production Conference, Cairo, Egypt, **2**, 23–50.

Abdelmaksoud A., Ewida H. F., El-Habaak G. H., Amin A. T., 2019: 3D structural modeling of the Upper Bahariya member in Abu-Gharadig oil and gas field, North Western Desert, Egypt. J. Afr. Earth Sci., **150**, 685–700, `doi: 10.1016/j.jafrearsci.2018.09.022`.

Abu El-Ata A. S. A., 1988: The relation between the local tectonics of Egypt and the plate tectonics of the surrounding regions using geophysical and geological data. In: EGS Proc. of 6th Ann. Meet., Cairo, 92–112.

Archie G. E., 1942: The electrical log resistivity log as an aid in determining some reservoir characteristics. Trans. AIME, **146**, 1, 54–62, `doi: 10.2118/942054-G`.

Asquith G. B., Gibson C. R., 1982: Basic Well Log Analysis for Geologists. The American Association of Petroleum Geologists (AAPG), Tulsa, Oklahoma, USA, 216 p.

Bayoumi A., Lotfy H., 1989: Modes of structural evolution of Abu-Gharadig Basin, Western Desert of Egypt as deduced from seismic data. J. Afr. Earth Sci., **9**, 2, 273–287, `doi: 10.1016/0899-5362(89)90070-5`.

Crain E. R., 1986: The Log Analysis Handbook: Quantitative log analysis methods, Vol. 1. PennWell, Tulsa, Oklahoma, USA, 91–95, 684 p.

Dolson J. C., Shann M. V., Matbouly S., Harwood C., Rashed R., Hammouda H., 2001: The Petroleum Potential of Egypt. In: Downey M. W., Threet J. C., Morgan W. A. (Eds.): Petroleum Provinces of the Twenty-First Century. American Association of Petroleum Geologists Memoir, **74**, 453–482, `doi: 10.1306/M74775C23`.

Dresser Atlas, 1982: Well logging and interpretation techniques; the course for home study. Houston, Dresser Industries Inc., 241 p.

EGPC, 1992: Western Desert oil and gas fields (A comprehensive overview). 11th EGPC Petroleum Exploration and Production Conference, Egyptian General Petroleum Corporation, Cairo, 431 p.

El-Sabbagh A., Tantawy A. A., Keller G., Khozyem H., Spangenberg J., Adatte T., Gertsch B., 2011: Stratigraphy of the Cenomanian–Turonian Oceanic Anoxic Event OAE2 in shallow shelf sequences of NE Egypt. Cretac. Res., **32**, 6, 705–722, `doi: 10.1016/j.cretres.2011.04.006`.

Farrag S., Mahmoud I., 2022: Petrophysical evaluation and geochemical characterization of Abu Roash F Member Abu Gharadig Basin, Western Desert, Egypt. International Petroleum Technology Conference, Riyadh, Saudi Arabia, February 21–23, 2022, IPTC-22187-MS, `doi: 10.2523/IPTC-22187-MS`.

Galford J., Quirein J., Westacott W., Witkowsky J., 2013: Quantifying organic porosity from logs. Paper presented at the SPWLA 54th Annual Logging Symposium, New Orleans, Louisiana, USA, June 22-26, 2013.

Hantar G., 1990: North Western Desert (chapter 15). In: Said R. (Ed.): The geology of Egypt. A. A. Balkema, Rotterdam, 293–319.

Ibrahim M., Abdel Aziz M., 1995: The Jurassic sediments in the Abu-Gharadig basin are promising reservoirs and source rocks. Proc. 12th EGPC Conference for Exploration and Production, Cairo, 248–252.

Katz B. J., 1995: A survey of rift basin source rocks. In: Lambiase J. J. (Ed.): Hydrocarbon Habitat in Rift Basins. Geol. Soc. Lond. Spec. Publ., **80**, 1, 213–240, `doi: 10.1144/GSL.SP.1995.080.01.11`.

Krygowski D. A., 2003: Guide to petrophysical interpretation. Austin Texas USA, 136 p.

Lüning S., Kolonic S., Belhadj E. M., Belhadj Z., Cota L., Barić G., Wagner T., 2004: Integrated depositional model for the Cenomanian–Turonian organic-rich strata in North Africa. Earth-Sci. Rev., **64**, 1-2, 51–117, `doi: 10.1016/s0012-8252(03)000 39-4`.

Luthi S. M., Souhaité P., 1990: Fracture apertures from electrical borehole scans. Geophysics, **55**, 7, 821–833, `doi: 10.1190/1.1442896`.

Meshref W., 1990: Tectonic Framework of Egypt. In: Said R. (Ed.): Geology of Egypt. Balkema/Rotterdam/Bookfield, Netherlands, 113–156.

Osman O. A., Hanafy A. G., Nour A. M., Benyamin M. H., Mostafa R. S., Eid R. E., Diab H. D., Redwan M. S., 2022: Integration of seismic attributes and borehole images for exploring the prospectivity of late Jurassic and early Cretaceous carbonates in north Western Desert, Egypt. ADIPEC, Abu Dhabi, UAE, October 31–November 3, 2022, SPE-211667-MS, `doi: 10.2118/211667-MS`.

Passey Q. R., Creaney S., Kulla J. B., Moretti F. J., Stroud J. D., 1990: A practical model for organic richness from porosity and resistivity logs. AAPG Bulletin, **74**, 12, 1777–1794, `doi: 10.1306/0C9B25C9-1710-11D7-8645000102C1865D`.

Philip J., Babinot J. F., Tronchetti G., Fourcade E., Ricou L. E., Guiraud R., Bellion Y., Herbin J. P., Combes P. J., Cornee J .J., Dercourt J., 1993: Late Cenomanian (94 to 92 Ma). In: Dercourt J., Ricou L. E., Vrielynck B. (Eds.): Atlas Tethys Palaeoenvironmental Maps. Gauthier-Villars, Paris, 153–178.

Rider M. H., 1996: Geological interpretation of well logs. Rider-French Consulting Ltd., Whittles Publishing, 280 p.

Schlumberger Ltd., 1972: Log Interpretations: Vol. 1 – Principles. Schlumberger Well Services, Houston, 113 p.

Schlumberger Ltd., 1995: Log Interpretation Charts. Houston, Texas.

Schmoker J. W., Hester T. C., 1983: Organic carbon in Bakken Formation, United States portion of the Williston Basin. AAPG Bull., **67**, 12, 2165–2174, `doi: 10.1306/AD46 0931-16F7-11D7-8645000102C1865D`.

Sheriff R. E., Geldart L. P., 1995: Exploration Seismology. Cambridge Univ. Press, 423 p.

Steiner S., Ahsan S. A., Raina I., Dasgupta S., Lis G. P., 2016: Interpreting Total Organic Carbon TOC in source rock oil plays. Abu Dhabi International Petroleum Exhibition & Conference, Abu Dhabi, UAE, November 7–10, 2016, SPE-183050-MS, doi: 10.2118/183050-MS.

Zobaa M. K., Oboh-Ikuenobe F. E., Ibrahim M. I., 2011: The Cenomanian/Turonian oceanic anoxic event in the Razzak field, North Western Desert, Egypt: Source rock potential and paleoenvironmental association. Mar. Pet. Geol., **28**, 8, 1475–1482, doi: 10.1016/j.marpetgeo.2011.05.005.